Vacancy infilling during the crystallization of Fe-deficient hematite: An in situ synchrotron X-ray diffraction study of non-classical crystal growth

SI ATHENA CHEN^{1,*}, PETER J. HEANEY¹, JEFFREY E. POST², PETER J. ENG^{3,4}, AND JOANNE E. STUBBS³

¹Department of Geosciences, Penn State University, University Park, Pennsylvania 16802, U.S.A.
 ²Department of Mineral Sciences, Smithsonian Institution, Washington, D.C. 20560, U.S.A.
 ³Center for Advanced Radiation Sources, The University of Chicago, Chicago, Illinois 60637, U.S.A.
 ⁴James Franck Institute, The University of Chicago, Chicago, Illinois 60637, U.S.A.

ABSTRACT

The crystallization of hematite from precursor ferrihydrite was studied using time-resolved, angle-dispersive synchrotron X-ray diffraction in aqueous solutions at pH 10 and 11 and at temperatures ranging from 80 to 170 °C. Rietveld analyses revealed a non-classical crystallization pathway involving vacancy infilling by Fe as defective hematite nanocrystals evolved. At 90 °C and pH 11, incipient hematite particles exhibited an Fe site occupancy as low as 0.68(2), and after 30 min, Fe occupancy plateaued at 0.84(1), achieving a metastable steady state with a composition corresponding to "hydrohematite." During crystal growth, unit-cell volume increased with an increase in Fe occupancy. The increase in Fe occupancy in hydrohematite was accomplished by deprotonation, resulting in a shortening of the long Fe-O(H) bonds and decreased distortion of the octahedral sites. Once the occupancy stabilized, the unit-cell volume contracted following further nanoparticle growth. Our study documented various synthetic routes to the formation of "hydrohematite" with an Fe vacancy of 10–20 mol% in the final product.

The structure refined for synthetic hydrohematite at 90 °C and pH 11 closely matched that of natural hydrohematite from Salisbury, Connecticut, with a refined Fe occupancy of 0.83(2). Dry heating this natural hydrohematite generated anhydrous, stoichiometric hematite, again by continuous infilling of vacancies. The transformation initiated at 150 °C and was complete at 700 °C, and it was accompanied by the formation of a minor amorphous phase that served as a reservoir for Fe during the inoculation of the defective crystalline phase.

Keywords: Hematite, 2-line ferrihydrite, crystal growth, time-resolved X-ray diffraction, kinetics

Introduction

Hematite (Hm) occurs as a naturally abundant coating on sediments and soils, often controlling the sorption and redox states of dissolved metals and organic pollutants (Barrón and Torrent 2013; Claudio et al. 2017). Hematite also has been used as a paleoclimate proxy for environments thousands to millions of years in the past, via hematite:goethite ratios (Ji et al. 2004; Hyland et al. 2015) and also as the primary carrier of natural remanent magnetization in redbeds, enabling plate tectonic reconstruction (e.g., Walker et al. 1981; Løvlie et al. 1984; Szaniawski et al. 2012). In addition, hematite is an important industrial material that is widely used in pigments, catalysts, batteries, sensors, photoelectrochemical water splitting devices, heavy-metal decontaminants, and many other applications (Paterson 1999; Walter 2006; Lu et al. 2014; McBriarty et al. 2018; Guo et al. 2020).

The presence of vacancies in hematite greatly enhances its efficiency as a photocatalyst (Guo et al. 2020), an adsorbent of radiotoxic elements (Wang et al. 2015; McBriarty et al. 2018), a charge-storage capacitor (Hahn et al. 2011; Lu et al. 2014), and

an electrical conductor (Yang et al. 2013). Many studies have focused on the effects of oxygen vacancies and surface iron deficiencies in hematite (Yang et al. 2013; Hu et al. 2016; Kim 2020). In this paper, we explore hematite that exhibits bulk Fe cation deficiencies.

The hematite structure (space group $R\overline{3}c$) contains sheets of oxygen anions that are hexagonal closest packed, and Fe fills ²/₃ of the octahedral sites (Blake et al. 1966). The substitution of 3H⁺ ↔ 1Fe3+ yields the following general formula for hydrohematite: $Fe_{2-x/3}(OH)_xO_{3-x}$ (Fig. 1). Wolska and Schwertmann (1989) designated the term "hydrohematite" for the compositional range $0.5 \ge x > 0$, and "protohematite" for $1 \ge x > 0.5$. "Protohematite" with Fe vacancies up to 10 mol% has been observed as an intermediate during the heating of goethite (Gualtieri and Venturelli 1999; Burgina et al. 2000). In their study of the transformation of akageneite to hematite, however, Peterson et al. (2015, 2016) reported transient hematite-like precursors with Fe vacancy concentrations greatly exceeding 10 mol%. Despite the importance of hematite for commercial, technological, and paleoenvironmental applications, little is known about its tolerance for Fe deficiencies and the range of Fe occupancies in natural and synthetic hematite minerals.

Figure 1 represents the Fe stoichiometries along a join con-

^{*} E-mail: siathenachen@gmail.com. Orcid 0000-0002-5391-4493

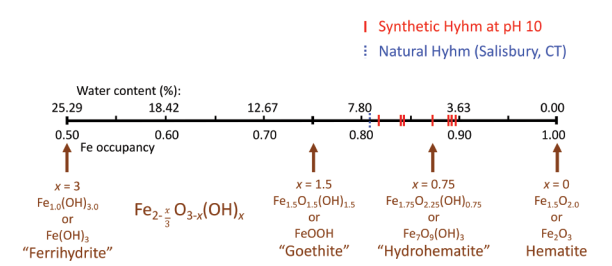


FIGURE 1. The compositional relationships among ferrihydrite, hydrohematite, and stoichiometric hematite. Synthetic hydrohematite products in this study exhibited refined Fe occupancies in the range of 0.80 to 0.90. (Color online.)

necting compositions extending from "ferrihydrite" [simplified to Fe(OH)₃] to end-member hematite (Fe₂O₃), all having the $R\overline{3}c$ symmetry of stoichiometric hematite. When only ${}^3\!\!/\!\!$ of the octahedral sites of hematite are filled (i.e., Fe_{occ} = 0.75), then the ratio of Fe to O is ${}^2\!\!/\!\!\!/\!\!\!$ s ${}^3\!\!/\!\!\!/\!\!\!/\!\!\!$ is elding a formula of FeOOH, with H serving to charge balance. To distinguish this phase from FeOOH-goethite with space group *Pnma*, we will describe " $R\overline{3}c$ hematite-type FeOOH" as "Hm-FeOOH" hereafter in this paper.

Despite the modern definition of "hydrohematite" introduced by Wolska and Schwertmann (1989), the mineral name actually was first proposed in the 1840s. Hermann (1844) and Breithaupt (1847) reported the discovery of hematite-like minerals with chemistries exactly halfway between the compositions of goethite and hematite, such that $Fe_{occ} = 0.875$. Hermann (1844) called this mineral "turgite" (a term now employed by collectors to describe iridescent goethite), and Breithaupt (1847) christened this phase "hydrohematite." In terms of crystallographic Fe occupancy, the "hydrohematite" of Wolska and Schwertmann (1989) includes compositions for which $1 > Fe_{occ} > 0.917$, whereas "protohematite" includes phases for which $0.917 > Fe_{occ} > 0.833$. Therefore, Breitmann's "hydrohematite" would be classified by Wolska and Schwertmann (1989) as "protohematite" rather than "hydrohematite."

Our analyses of Fe-deficient hematite-like phases from historical collections (Chen et al. 2021) revealed that Fe occupancies are highly variable in natural specimens. Despite the groundbreaking character of the studies by Wolska and coworkers (Wolska 1981, 1988; Wolska and Schwertmann 1989), we regard their revised nomenclature as historically problematic. In this article, we use the term "superhydrous hematite" to represent $R\overline{3}c$ structures over the range of stoichiometries between Fe(OH)₃ and Fe₂O₃ (Fig. 1). Although the International Mineralogical Association has not approved the name "hydrohematite" for any usage, we will employ hydrohematite (without quotations) to refer to compositions that lie halfway between those of Fe₂O₃ and FeOOH—formally, near Fe₇O₉(OH)₃ (Fig. 1).

We have performed a detailed atomic-scale study of the transformation of 2-line ferrihydrite to hydrohematite, and hydrohematite to end-member hematite, by time-resolved synchrotron X-ray powder diffraction (TRXRD). Using freshly prepared ferrihydrite in alkaline (pH 10, 11) solutions as the starting material, we synthesized metastable Fe-deficient hydrohematite over a range of temperatures and monitored Fe occupancy parameters as nanocrystalline hematite evolved.

To further explore the metastability of hydrohematite, we dryheated natural hydrohematite and documented its conversion to stoichiometric hematite. Our study highlights a non-classical crystallization mechanism involving vacancy inoculation with Fe during crystal growth, and it demonstrates that hematite can accommodate high concentrations of Fe vacancies and maintain structural integrity. The exceptionally Fe-deficient hydrohematite phases that we observed have the potential to tolerate high levels of dopants in their structures and to serve as candidate materials for adsorbents and photoelectrochemical energy conversion devices. In addition, they will exhibit magnetic properties that markedly depart from those observed in end-member hematite (Hill et al. 2008; Jiang et al. 2022).

EXPERIMENTAL METHODS

Ferrihydrite preparation

Ferrihydrite was the starting material for hydrohematite crystallization. Fresh ferrihydrite was prepared at room temperature using the method described by Cornell and Schwertmann (2003). We dissolved 4.039 g iron nitrate nonahydrate [Fe(NO₃)₃·9H₂O] in 10 mL deionized water to produce a 1 *M* solution of Fe(NO₃)₃. This solution was titrated with 5 *M* KOH drop by drop until the pH held steady for >10 min at pH 10 and 11. The drop-by-drop titration was completed after about 40 min. Two-line ferrihydrite, as identified by synchrotron X-ray diffraction, precipitated as a gel (containing ~0.5 *M* ferrihydrite) immediately upon the reaction of the Fe(NO₃)₃ and KOH. We used this fresh ferrihydrite (aged no longer than 4 h) as the reaction precursor. When the ferrihydrite aged longer than 24 h at room temperature, X-ray diffraction (XRD) patterns still revealed 2-line ferrihydrite, but the aged ferrihydrite failed to transform to either hematite or goethite upon heating at 80 to 170 °C for at least 12 h. Therefore, we utilized freshly prepared ferrihydrite for all of our TXRD experiments.

Using a 1 mL syringe, we injected ferrihydrite gel into a thin-walled quartz glass capillary (40 mm long and 1.0 mm outer diameter; Charles Supper Company). UV-cured epoxy (OG142-87, EPO-TEK) was then injected to seal the capillary. The epoxy caps were cured using a full-spectrum UV lamp (EXFO X-Cite Series 120). The ferrihydrite gels were masked during this step to minimize interaction of UV light with the gels, and each capillary was rotated during curing to ensure even curing of the epoxy. The volumes of the ferrihydrite gels ($\sim\!30~\mu\text{L}$), the aging times of the gels (within 4 h), and the amount of headspace in the capillary (1 mm away from the top of the gel surface) were maintained as similar as possible to minimize sample variations. Capillaries were inserted into a standard Cu brass mounting pin for loading in an X-ray goniometer head. The capillary was secured within the brass pin by a small amount of clay.

Time-resolved synchrotron X-ray diffraction (TRXRD)

TRXRD patterns were collected at the GeoSoilEnviroCARS (GSECARS) 13-BM-C beamline at the Advanced Photon Source (APS), Argonne National Laboratory (ANL). The monochromatic X-ray wavelength was refined as 0.8291(5) Å using a LaB₀ standard. The distance from the sample to the camera was refined to be 108.45(6) mm. The partially focused X-ray beam measured ~0.3 mm in height and 0.4 mm in width, and it was directed to the center of the capillary. Capillary orientation was maintained perpendicular to the forced-gas heater (described below). Capillaries were rotated 30° about their long axes at 1° per second to minimize preferred orientation effects in the XRD patterns. Each pattern was collected with an exposure time of 30 s using either a MAR 165 CCD detector or a Dectris PILATUS 1M pixel array detector. Full-circle images were integrated into linear intensity-vs.-2θ XRD data sets using the program Dioptas (Prescher and Prakapenka 2015).

Electrically resistive forced helium heaters

A low-temperature forced-gas heater was fabricated at GSECARS for heating experiments below 250 °C, similar to the one described by Heaney et al. (2020). This low-temperature heater consisted of wound Ni coils around an inner ceramic tube, with an applied DC voltage using a Sorensen 33 V \times 33 A (Model XHR 33-33) power supply to achieve resistive heating. This assembly was encased in an outer ceramic sleeve, and He gas was forced through the interior of the heated cylinder.

A second forced-gas heater was fabricated for high-temperature heating experiments from room temperature to 1000 °C. The design of this high-temperature heater was nearly identical to that of the low-temperature heater but used freestanding W coils instead of Ni wound around a central ceramic support.

Both heaters were placed below the capillary with the gas flowing out of a 6 mm nozzle directed perpendicular to the capillary's long dimension and centered on the region where XRD measurements were made. The temperature was measured by placing the tip of a type-K thermocouple into the center of the He gas flow $\sim\!3$ mm from the heater's exit and a few millimeters from the capillary. The temperature was monitored with a Keithley 2700 Multimeter. We heated samples from room temperature to the target temperature using proportional-integral-derivative (PID) software. The low-temperature furnace heated at a rate of 14 °C/s, such that the target temperatures were achieved in a few seconds before the start of the second pattern, and these temperatures stabilized at ± 0.5 °C.

Temperature was calibrated using phase transitions of RbNO₃ (Alfa Aesar, 99.8%, metals basis) and the melting point of metallic silver for both heaters. We monitored the transformation of RbNO₃ loaded in a 1.0 mm quartz glass capillary and heated from 25.7 to 400 °C. Based on this standardization, we estimate that the temperature measured by the thermocouple was within ± 1.5 °C of the actual temperature inside the capillary.

Heating temperatures

For experiments involving the low-temperature hydrothermal transformation of ferrihydrite to hydrohematite, runs were conducted using the low-temperature heater at the following constant temperatures: 80, 90, 100, 110, 130, 150, and 170 °C, all at pH 10, and 90 °C at pH 11. We terminated data collection after reaction progress ceased, with run times of 9, 2, 1.5, 1, 1, 0.5, 2, and 1.6 h, respectively. Individual two-dimensional diffraction patterns were collected for 30 s, and we allowed 8 s for software integration of the 2-dimensional ring patterns into one-dimensional intensity- vs.-20 patterns, for a total data collection time of 38 s per XRD pattern.

To analyze the transformation of hydrohematite to hematite, we used the high-temperature furnace to heat dry natural hydrohematite powders from Salisbury, CT (Genth 255-3, Chen et al. 2021) according to the following schedule: (1) initial heating up to 90 °C at 13 °C/min; (2) ramping from 90 to 1000 °C at 2 °C /min; and (3) sustained heating at 1000 °C for 0.5 h, to match the protocol of Gualtieri and Venturelli (1999). We loaded the natural hydrohematite powders from Salisbury in a 0.7 mm thin-walled quartz capillary with one end unsealed to allow for the release of water vapor and other gases during heating. The diameter of the quartz capillary in the high-temperature dry heating experiment was smaller than that used in our low-temperature hydrothermal experiments, 0.7 vs. 1.0 mm, because of the significantly higher X-ray absorption by the well packed dry powders.

Rietveld structure refinement

Rietveld structure refinements were performed using the EXPGUI interface of the General Structure Analysis System (GSAS) program (Larson and Von Dreele 2000; Toby and Von Dreele 2013). The starting structural parameters for hematite (space group R3c), goethite (space group Pnma), and magnetite (space group Fd3m) came from Blake et al. (1966), Gualtieri and Venturelli (1999), and Haavik et al. (2000), respectively. The Gaussian peak shape coefficients GU, GV, and GW were determined by refinement of a LaB6 standard analyzed at the start of our data collection and fixed for the remainder of the refinements. First, we refined the background, weight fraction, sample displacement, and unit-cell parameters. Backgrounds were best fit for all patterns using a shifted Chebyschev polynomial with 12 terms. Peak profiles were modeled using a pseudo-Voigt function described by Thompson et al. (1987). Second, the profile parameters sensitive to crystal size broadening (LX), strain broadening (LY), anisotropic crystal size broadening (ptec), and anisotropic microstrain broadening (S_{hkl}) were refined. After the above parameters had converged, atomic positions, and finally Fe occupancies in hematite were allowed to refine. When the refinement of isotropic temperature factors ($U_{\rm iso}$) generated negative values, values for $U_{\rm iso}$ were fixed to 0.006 for Fe and 0.012 for O.

Refinements were performed over a d-spacing range from 1.36-5.94 Å $(35.50^{\circ}$ to 8.00° 20). Goodness-of-fit parameters indicated high-quality refinements (Online Materials¹ Fig. S1), with χ^2 ranging from 0.1 to 1.2 (± 0.03 to 0.05), R_{wp} from 0.001 to 0.005 (± 0.001 to 0.002), and R_{Bragg} from 0.010 to 0.014 (± 0.001 to 0.002).

Crystallite size determination

We estimated the crystallite size using the Scherrer (1918) equation:

$$\tau = K \lambda / \beta \cos \theta \tag{1}$$

where τ is the mean particle size; K is the crystal shape factor, in this case, 0.9 (Bagheri et al. 2013); β is the full-width at half maximum of a Bragg peak (FWHM, corrected for instrumental broadening by a LaB $_6$ standard); λ is the X-ray wavelength; and θ is the Bragg angle. To account for instrumental broadening, the FWHM of the (211) diffraction peak of a LaB $_6$ standard was measured using the MDI JADE 2010 software (Materials Data, Inc. Livermore, California), and that value was subtracted from the FWHM of the (116) diffraction peak of the emergent hydrohematite.

RESULTS

Transformation pathway

Two-line ferrihydrite (Fh) transformed to hydrohematite (Hyhm) and goethite (Gt) in all of our experiments. Despite prior reports that this reaction sequence involves a maghemitelike phase as an intermediate (Barrón et al. 2003; Cao et al. 2017), diffraction peaks for maghemite were never detected in any of our experiments. A representative TRXRD sequence (90 °C and pH 11) is shown in Figure 2 and a complimentary stacked 2D plot (intensity vs. 2θ and d-spacing) is shown in Online Materials¹ Figure S2. Precursor 2-line ferrihydrite is indicated by two broad peaks at 2.54 and 1.46 Å. Within a data collection time of 38 s, the strongest diffraction peak for hydrohematite (104) typically appeared shortly before (within 2 min of) the appearance of the strongest goethite peak (101). One should note, however, that hematite diffracts more strongly than does goethite; the reference intensity ratio (RIR) for hematite is 3.18, whereas that for goethite is 2.63 (Gates-Rector and Blanton 2019). Moreover, the peak-to-background ratios for these emergent phases are extremely low. Despite these uncertainties, our analyses from the suite of experiments consistently suggested that hydrohematite precipitates from ferrihydrite slightly sooner than goethite.

The refined weight fractions and normalized scale factors as a function of time for 90 °C and pH 11 are plotted in Figure 3. Scale factors directly reflect the mass of each phase as detected by the X-ray beam within the sampling window. To compare the behaviors of hematite and goethite, the scale factors were normalized to their final refined values for each phase at the end of the experiment. As seen in Figure 3a, both hydrohematite and goethite continuously increased in mass abundance until attaining a plateau when ferrihydrite was depleted (~3500 s in Fig. 3a). Despite the first appearance by hematite, the weight fraction (Fig. 3b) of goethite dominated in the earliest stages of each run but was overtaken by hematite. At 90 °C and pH 11, the experimental systems achieved a steady state with ~75 wt% hematite and ~25 wt% goethite. As seen in Figure 3b, this hematite-to-goethite ratio was maintained despite continued co-precipitation of goethite and hematite, as reflected in the refined scale factors beyond 1000 s in Figures 3a and 3b. We attribute the constancy of these phase proportions to a uniformity in the kinetics of precipitation, which depend strongly on pH and temperature (Chen 2021). In agreement with Das et al. (2011), goethite growth was more favorable at low temperatures (Table 1).

Fe occupancy in hydrohematite

As shown in Figure 3, when ferrihydrite at pH 11 was heated to 90 °C, the Fe occupancy initially refined to 0.68(2) at 17 min and increased to 0.84(1) at 30 min. For the next 60 min, Fe_{occ}

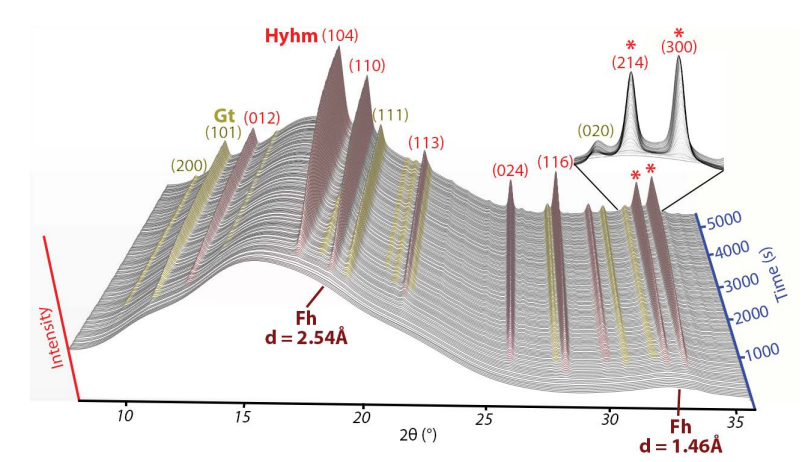


FIGURE 2. Stacked TRXRD patterns showing the crystallization of hydrohematite (Hyhm, red peaks) and goethite (Gt, yellow peaks) from 2-line ferrihydrite (Fh) at 90 °C pH 11. Zoom-in plot showed that the ratio of starred peaks at (214) (left) and (300) (right) in hydrohematite is sensitive to time and Fe occupancies. (Color online.)

stabilized at 0.84. Although peak-to-background was low and errors were accordingly high for structure refinements of the first-formed crystals, our analyses revealed that Fe occupancies of incipient nuclei ranged between 0.60(2) and 0.75(2)—below that of Hm-FeOOH. Estimated standard deviations (ESDs) for refined occupancies as calculated during Rietveld refinements typically are underestimated (Post and Bish 1989). Experiments at other temperatures, however, exhibited similar behaviors (Online Materials¹ Fig. S3), such that hydrohematite started with iron occupancies below 0.75(2), and then evolved to a metastable hydrohematite composition by Fe infilling during crystal growth.

The refined Fe occupancies for the final metastable hydrohematite structures ranged from 0.80–0.90 in our experiments (Table 2; Fig. 1). Though we were time-limited during our synchrotron runs, our experiments demonstrated that highly Fe-deficient hydrohematite remained unchanged for more than 4 h when temperatures were lower than 150 °C. Prior researchers have observed Fe-deficient hematite-like phases as unstable, intermediate precursors during stoichiometric hematite formation (Gualtieri and Venturelli 1999; Peterson et al. 2018). For the first time, we have shown that at pH 10 and 11, ferrihydrite gels will generate hydrohematite with Fe occupancies ranging from 0.80–0.90 as a steady-state product (Figs. 3 and 4; Online Materials¹ Fig. S3).

In Figure 4, we have plotted the Fe occupancy of hematite as a function of reaction time and temperature for all runs at pH 10 from 80–170 °C. This plot shows the Fe concentration of hydrohematite at different time stamps at various temperatures. A 2D projection of Figure 4 is shown in Online Materials¹ Figure S4. At pH 10, higher temperatures favor hydrohematite with fewer

TABLE 1. The weight fraction of hydrohematite (Hyhm) and goethite (Gt) and Rietveld fitting parameters at pH 10 from $80-170\,^{\circ}$ C and pH 11 from $90\,^{\circ}$ C

| | | | Wt, fra | (| Goodness of Fit (GOF) | | | | | |
|---------------------------------------------------------------|----|--------------------|---------|---------|-----------------------|------|--------|-----------------|--|--|
| T (°C) | рΗ | Heating time (min) | Hyhm | Gt | | χ² | wRp | RF ² | | |
| 80 | 10 | 50 | 0.67(1) | 0.33(1) | 0. | 6486 | 0.0070 | 0.1336 | | |
| 90 | 10 | 18 | 0.78(1) | 0.22(1) | 0. | 7221 | 0.0072 | 0.0928 | | |
| 110 | 10 | 44 | 0.88(1) | 0.12(1) | 0. | 3500 | 0.0055 | 0.0423 | | |
| 130 | 10 | 30 | 0.79(1) | 0.21(1) | 0. | 6502 | 0.0060 | 0.0709 | | |
| 150 | 10 | 7 | 0.84(1) | 0.16(1) | 0. | 6680 | 0.0060 | 0.0711 | | |
| 170 | 10 | 7 | 0.90(1) | 0.10(1) | 0. | 2138 | 0.0046 | 0.0523 | | |
| 90 | 11 | 90 | 0.71(1) | 0.29(1) | 0. | 9786 | 0.0079 | 0.2185 | | |
| ^a Weight fractions were constrained to sum to 1.0. | | | | | | | | | | |

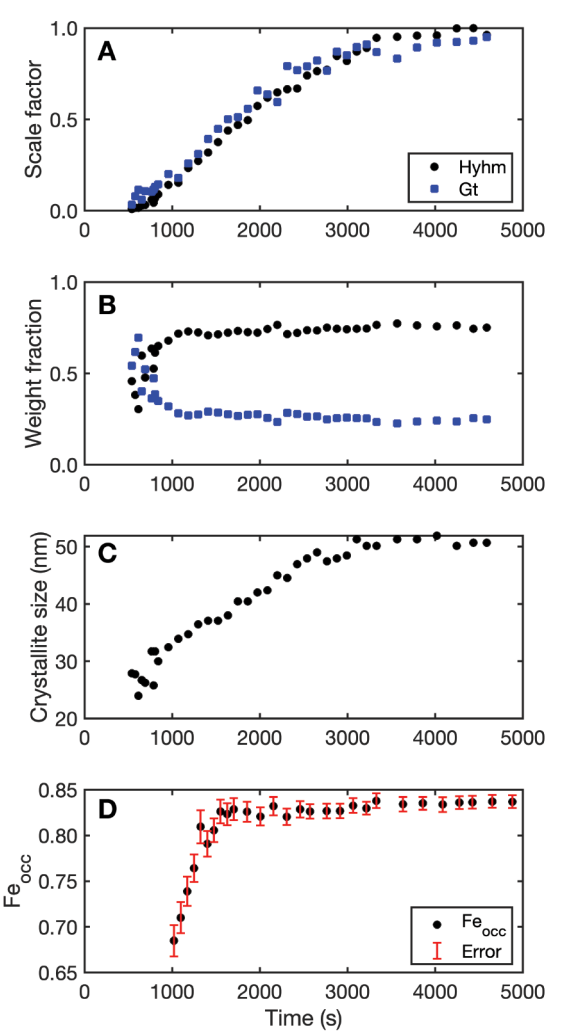


FIGURE 3. (a) A representative refinement at 90 °C and pH 11 showed that hydrohematite (Hyhm, black dots) and goethite (Gt, blue squares) precipitated from ferrihydrite with time. (b) Normalized scale factors and (c) crystallite sizes achieved a plateau at ~3300 s, indicating that ferrihydrite had depleted and crystal growth ceased. (d) Refined Fe occupancy in hematite (Chen et al. 2021) increased from 0.68(2) to 0.84(1) after 1550 s, and then stabilized at 0.84(1), suggesting metastable hydrohematite formed. Rietveld refined standard deviations were smaller than symbols. (Color online.)

| <i>T</i> (°C) p | На | Heating time (min) | | Hydrohematite | | | Goethite | | | | |
|-----------------|----|---------------------|----------|---------------|------------|-------------------|----------|----------|----------|----------|------------|
| | рп | rieating time (min) | a (Å) | c (Å) | Volume (ų) | Fe _{occ} | | a (Å) | b (Å) | c (Å) | Volume (ų) |
| 80 | 10 | 50 | 5.032(1) | 13.748(1) | 301.51(3) | 0.82(1) | | 9.946(2) | 3.019(1) | 4.603(1) | 138.22(4) |
| 90 | 10 | 18 | 5.031(1) | 13.747(1) | 301.35(3) | 0.84(1) | | 9.950(2) | 3.021(1) | 4.602(1) | 138.34(4) |
| 110 | 10 | 44 | 5.034(1) | 13.757(1) | 301.96(3) | 0.89(1) | | 9.964(2) | 3.024(1) | 4.600(1) | 138.58(4) |
| 130 | 10 | 30 | 5.044(1) | 13.780(1) | 303.60(3) | 0.89(1) | | 9.976(1) | 3.037(1) | 4.610(1) | 139.69(4) |
| 150 | 10 | 7 | 5.039(1) | 13.766(1) | 302.72(3) | 0.87(1) | | 9.945(1) | 3.026(1) | 4.607(1) | 138.66(4) |
| 170 | 10 | 7 | 5.038(1) | 13.763(1) | 302.57(3) | 0.89(1) | | 9.972(1) | 3.023(1) | 4.608(1) | 138.90(4) |
| 90 | 11 | 90 | 5.041(1) | 13.777(1) | 303.23(3) | 0.84(1) | | 9.965(1) | 3.025(1) | 4.612(1) | 139.04(4) |

TABLE 2. Rietveld refinement lattice parameters of metastable hydrohematite and goethite synthesized at pH 10, 11 in the present study

Fe vacancies, suggesting that highly Fe-deficient hematite, with Fe_{occ} = 0.8–0.9, is evidence of precipitation at temperatures less than 200 °C. In a separate study, we showed that stoichiometric hematite forms in acidic solutions (pH \leq 5) at high temperatures ($T \geq 180$ °C) (Chen et al. 2022).

Changes in unit-cell parameters and crystal size during hydrohematite growth

We monitored structural changes during the transformation from ferrihydrite to hydrohematite by combining synchrotron TRXRD and Rietveld analysis. The growth of hydrohematite nanoparticles was accompanied by an initially rapid expansion of the unit cell, followed by a decrease in the magnitudes of a and c, and therefore, of unit-cell volume (Fig. 5). The initial unit-cell expansion strongly correlated with an increase in Fe occupancy. We hypothesize that with higher occupancies of Fe, the Fe-Fe repulsion between adjacent face-sharing octahedra increased, resulting in the observed unit-cell expansion. The c-axis, which is normal to the plane of closest packed oxygen atoms, exhibited a more dramatic extension than did the a-axis. For example, at 90 °C and pH 11, as the Fe occupancy increased from 0.68(2) to 0.84(1) in the first 25 min, the c-axis expanded 0.050% while the a-axis expanded 0.023%, and unit-cell volume increased 0.083%. As described in more detail below, the greater expansion along c relative to a was associated with a larger change in the Fe-O-Fe angle of face-sharing octahedra along the c-axis than in the edge-sharing octahedra perpendicular to c. This unit-cell expansion continued until the crystallite sizes attained ~36 nm, as ascertained by Scherrer analysis.

Once the Fe occupancy achieved a steady state of ~ 0.85 , mean crystallite sizes continued to increase, and the unit-cell volume contracted. During this second stage, the a-axis contracted relatively more than the c-axis. Specifically, when hydrohematite

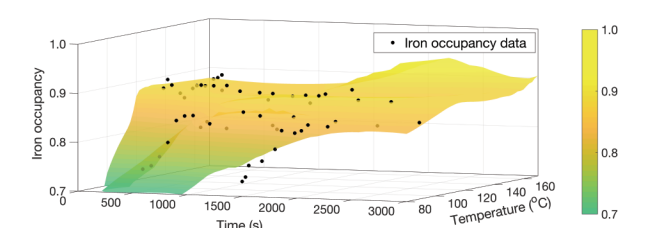


FIGURE 4. The dependence of Fe occupancy on transformation time and temperature (80–170 °C) as revealed by a best fit surface to our refined TRXRD data at pH 10. Our refined Fe occupancy data are indicated by black dots. Initial structures for hydrohematite were always highly Fe-deficient and then stabilized at a refined Fe occupancy of 0.8–0.9. Higher temperatures produced metastable hydrohematite with fewer Fe vacancies. (Color online.)

nanoparticles grew from \sim 37 to \sim 50 nm at 90 °C and pH 11, the Fe occupancy remained at 0.84(1), the *a*-axis contracted 0.065%, but the *c*-axis contracted only 0.025%. The decrease in lattice parameters during hydrohematite nanocrystal growth is consistent with the crystallization behavior of many other ionic nanoparticles (Perebeinos et al. 2002; Fischer et al. 2018; Diehm et al. 2012), although the cause of this inverse relationship remains controversial (Heaney et al. 2020).

Unit-cell volume, crystallite size, and scale factors plateaued at the same time in our experimental runs (~3300 s in Figs. 3

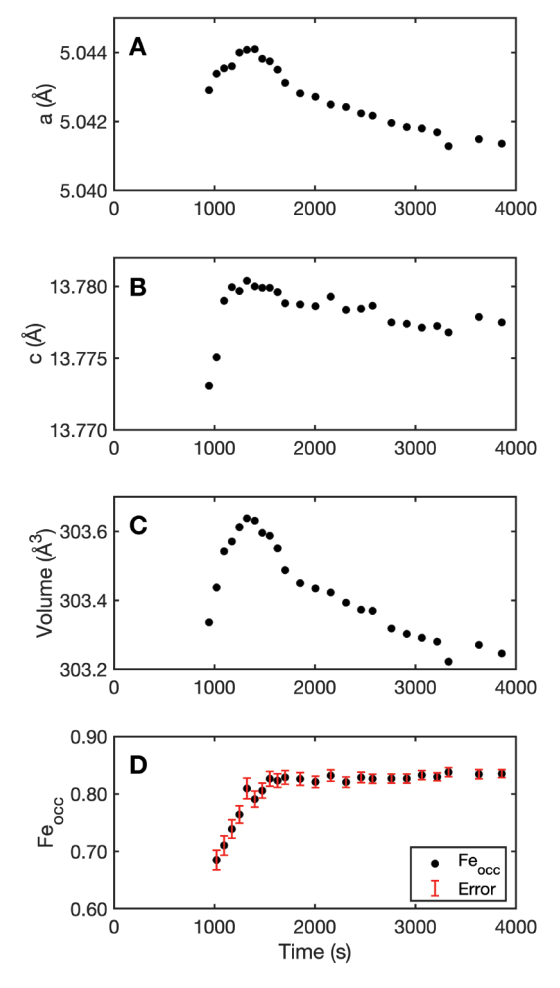


FIGURE 5. Evolution of unit-cell parameters a (a), c (b), and volume (c) during hydrohematite growth at 90 °C pH 11. Changes in Fe occupancy are included (d) (Chen et al. 2021) for comparison. Refinement errors, as reported by GSAS, are smaller than symbols. (Color online.)

American Mineralogist, vol. 108, 2023

and 5), indicating that depletion of ferrihydrite induced a cessation in crystal growth. The attainment of a steady-state value for Fe occupancy occurred much earlier than the termination of crystal growth. This result suggests that the generation of Fedeficient hydrohematite was favored relative to stoichiometric hematite in our experiments. Chen et al. (2021) reported a crystal structure for natural hydrohematite from Salisbury, CT. The final structure refined for synthetic hydrohematite at pH 11, 90 °C (Table 2) was nearly identical to that of the natural material, which exhibited a refined Fe occupancy of 0.83(2), *a*-axis of 5.040(1) Å, and *c*-axis of 13.797(1) Å.

Geometrical evolution of octahedral sites

For the end-product hydrohematite synthesized at pH 11 and 90 °C, the three longer Fe-O bonds refined as 2.164(4) Å, and the three shorter Fe-O bonds refined as 1.916(3) Å (Fig. 6). Blake et al. (1966), however, report that in stoichiometric hematite, the three longer Fe-O bonds are 2.119(2) Å and the three shorter Fe-O bonds are 1.941(2) Å. The duality of Fe-O bond lengths in the FeO₆ octahedra of hematite is attributed to Fe-Fe repulsion in face-sharing octahedra. In Fe-poor hydrohematite, the distortion associated with Fe-Fe repulsion, therefore, is diminished, but the octahedral site geometries also are influenced by OH⁻ groups. The long Fe-O bond lengths that we refined for hydrohematite reflect a 15% contribution of octahedral vacancy sites as well as a reduced effective charge for O in OH⁻. The average Fe-O bond lengths refined here for hydrohematite [2.040(2) Å] are not significantly different from the stoichiometric hematite

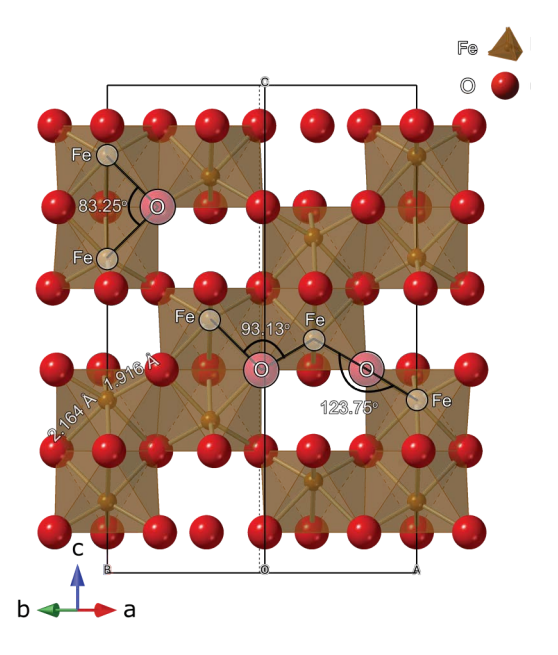


FIGURE 6. The crystal structure of hydrohematite synthesized at pH 11 and heated at 90 °C for 1.5 h, with a refined Fe occupancy of 0.84(1). The hydrohematite structure exhibits sheets of oxygen (O) anions that are hexagonal closest packed, and iron (Fe) resides within octahedral sites. Two types of Fe-O bonds refined as 2.164(4) and 1.916(3) Å. The Fe-O-Fe angles of face-sharing, edge-sharing, and corner-sharing octahedra are 83.25°(24), 93.13°(7), and 123.75°(32), respectively. (Color online.)

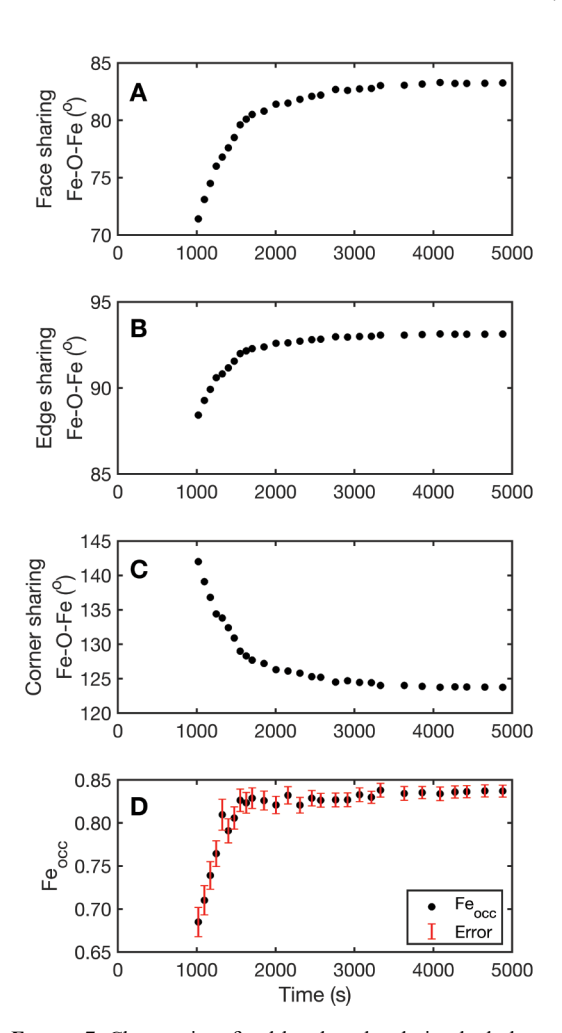


FIGURE 7. Changes in refined bond angles during hydrohematite growth at 90 °C pH 11. (a) The Fe-O-Fe angle reflects octahedra that are adjacent along the *c*-axis. These face-sharing octahedra exhibited the greatest expansion (16.65%) of all Fe-O-Fe and O-Fe-O angles. (b) The Fe-O-Fe angle represent adjacent octahedra within the (001) plane. These edge-sharing octahedra exhibited a smaller expansion of 5.34%. (c) The Fe-O-Fe angle of corner-sharing octahedra contracted 14.77%. Standard deviations of refined values are smaller than symbols. (d) Refined Fe occupancy in hematite (Chen et al. 2021) at 90°C and pH 11. (Color online.)

[2.030(2) Å] (Blake et al. 1966). We provide a full CIF file of our representative synthetic hydrohematite structure at pH 11 and 90 °C in the Online Materials¹, but we acknowledge that our neutron diffraction refinements in a separate study will present the magnetic structure and hydrogen positions of natural hydrohematite (Chen 2021).

Figure 7 offers some insight into the evolution of Fe-O octahedra during hydrohematite crystal growth. As Fe occupancy increased from 0.68(2) to 0.84(1), the Fe-O-Fe angle of the face-sharing octahedra increased 16.6% [from 71.4°(5) to 83.25°(24)]; the Fe-O-Fe angle of edge-sharing octahedra increased 5.4% [from 88.4°(3) to 93.13°(7)]; and the Fe-O-Fe angle for corner-sharing octahedra decreased 14.7% [from 142.0°(9) to 123.75°(32)]. These trends of Fe-O-Fe angles vs. Fe occupancies

are consistent with those described in Gualtieri and Venturelli (1999) for the transition of hydrohematite to stoichiometric hematite during the dry heating of goethite powders.

The greater expansion in the Fe-O-Fe angle oriented along c for face-sharing octahedra relative to the Fe-O-Fe angle between edge-sharing octahedra would be expected as Fe infills sites and Fe-Fe repulsion increases. Consequently, expansion along the c-axis is more significant relative to a, as described above. An animation of the structural changes observed during the evolution of hydrohematite at 90 °C and pH 11 is accessible in the Online Materials¹. This movie reveals that as the Fe occupancy for hydrohematite increases from \sim 0.68 to \sim 0.84, the FeO₆ octahedra develop from distorted to highly symmetrical coordination polyhedra when viewed along c.

Thermal stability of hydrohematite

We have reported natural occurrences of hydrohematite that likely persisted at low temperatures for hundreds of millions of years (Chen et al. 2021). Can hydrohematite diagenetically transform to stoichiometric hematite? To test the stability of hydrohematite, we dry-heated some hydrohematite samples from room temperature to 1000 °C using TRXRD (Figs. 8 and 9). Because our synthetic hydrohematite contained low concentrations of goethite, we employed phase pure natural hydrohematite from Salisbury, Connecticut (Penn State University, Genth Collection no. 255.3). A complete structure refinement of Salisbury hydrohematite has been reported in Chen et al. (2021).

Rietveld refinement allowed us to explore the changes in structure and Fe occupancy with elevated temperatures. The refined Fe occupancy of Salisbury (Connecticut) hydrohematite before heating was 0.81(1) (Fig. 9), within the error of the value reported in Chen et al. (2021) of 0.83(2). The Fe occupancy increased very slightly from room temperature to ~150 °C, beyond which the rate of Fe infilling was notably more rapid (Fig. 10). Above 200 °C, the refined Fe occupancy increased linearly with temperature until Fe_{occ} achieved unity at 700 °C (Fig. 10g). Magnetite appeared at 400 °C due to the reduction of Fe³⁺ to Fe²⁺, but only in small quantities, representing <2 wt% of the mixture at 700 °C.

The transformation from hydrohematite to stoichiometric

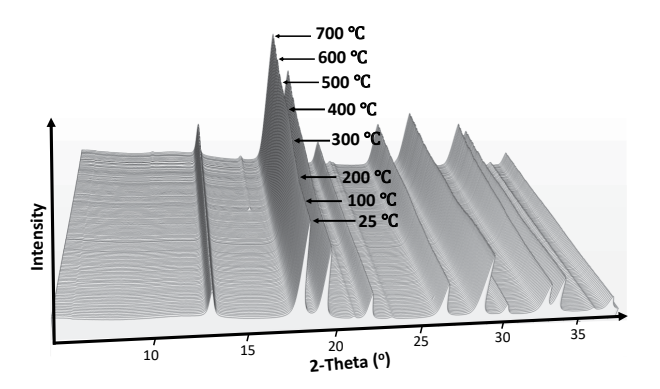


FIGURE 8. Stacked TRXRD patterns showing the transformation of hydrohematite to hematite when dry heated from room temperature to 700 °C.

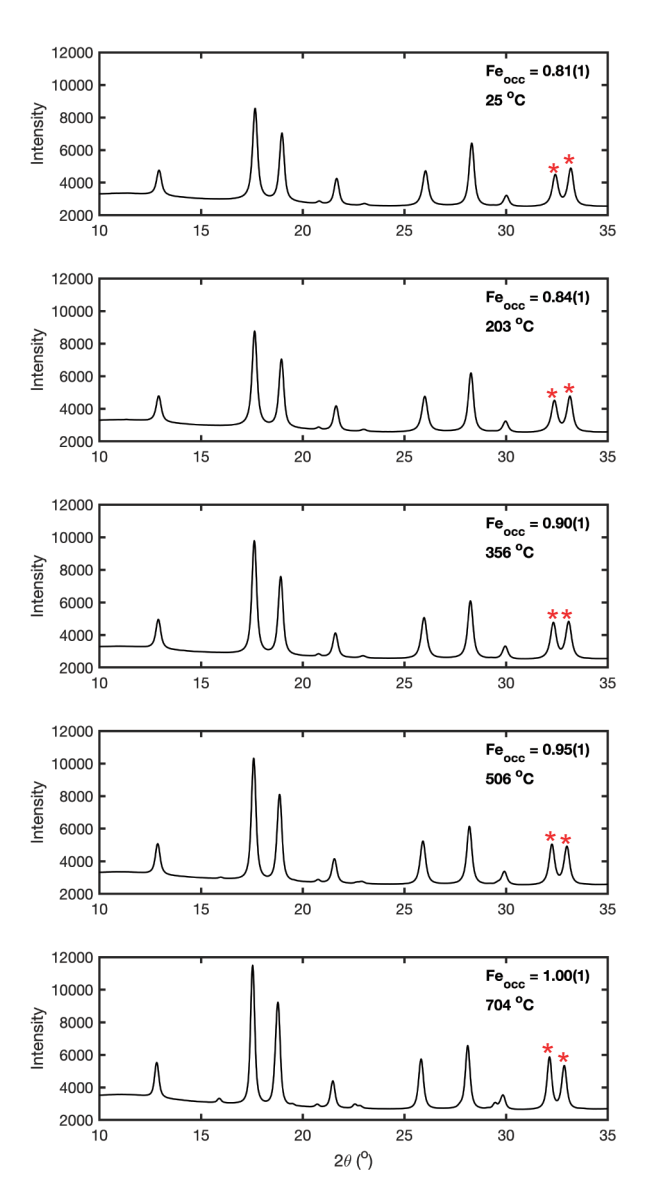


FIGURE 9. XRD patterns with varied Fe occupancies during the transformation of hydrohematite to hematite. The ratio of starred peaks at (214) and (300) is sensitive to Fe occupancies. (Color online.)

hematite was accompanied by measurable structural changes. Consistent with our synthetic hydrohematite, within each FeO₆ octahedron in Salisbury hydrohematite, two types of Fe-O bonds exist, with refined distances of 2.154(2) Å and 1.923(2) Å at room temperature. Between room temperature and 150 °C, the overall thermal expansion induced a stretching of all Fe-O bond lengths and an increase in unit-cell volume with scarcely any change in Fe occupancy (Fig. 10). When the temperature exceeded 150 °C, however, hydrohematite started to lose hydroxyls with a concomitant increase in Fe occupancy. At the onset of this dehydration, we observed a decrease in refined crystallite size and a rapid increase in the Fe-Fe bond length. Despite the overall thermal expansion that accompanied heating, the long Fe-O bond contracted in response to deprotonation. From 150 to 400 °C, the dehydration

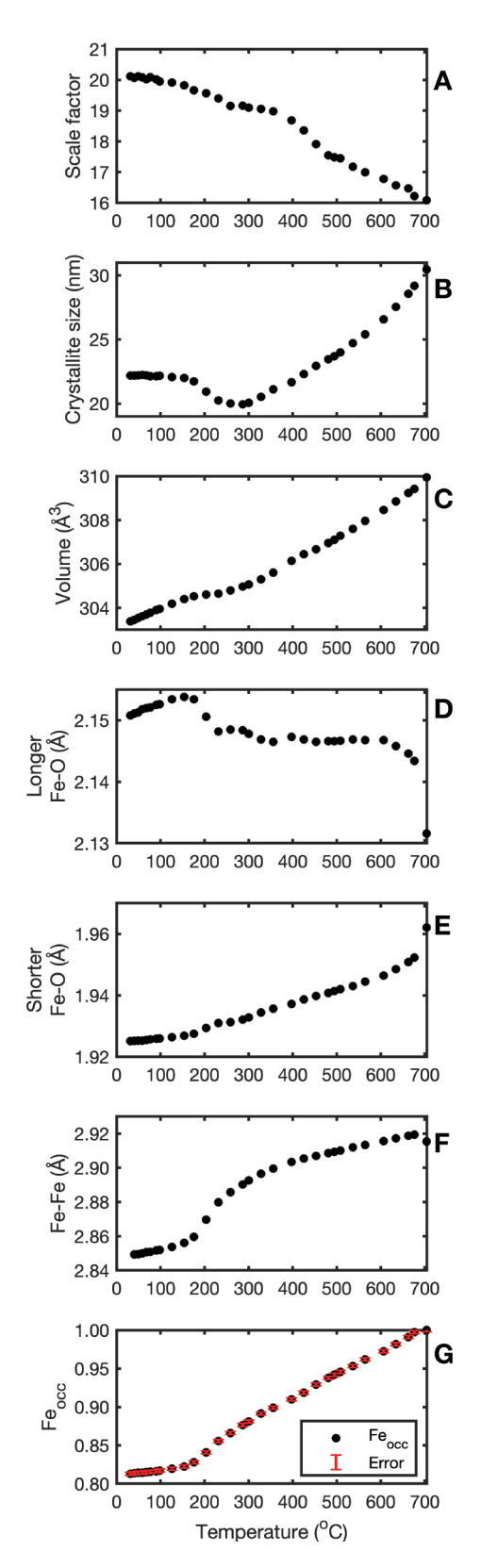


FIGURE 10. Crystallographic evolution in the transformation of hydrohematite to hematite with increased temperatures. Standard deviations of refined values are smaller than symbols. (Color online.)

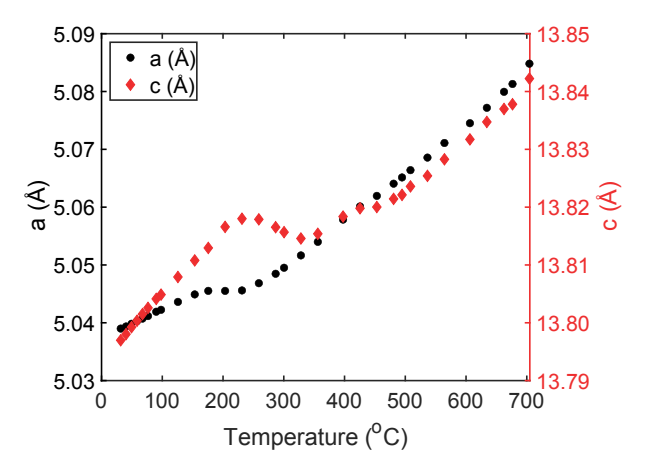


FIGURE 11. Refined lattice parameters in the dehydration of hydrohematite to hematite with increased temperatures. (Color online.)

process dominated the thermal expansion such that the unit-cell expansion slowed and, even more dramatically, c contracted between 230 and 330 °C (Fig. 11). These crystallographic changes between 150 and 400 °C are consistent with a significant water loss, as further supported by thermogravimetric analysis-mass spectroscopy (TGA-MS) analysis (Chen et al. 2021). Moreover, crystal annealing was revealed by the sustained increase in crystallite size from 300 to 700 °C.

From 400–600 °C, the refined Fe occupancy increased from \sim 0.91 to \sim 0.96, and all lattice parameters continued to expand. The long Fe-O bond length was constant within error, but the short Fe-O bond increased due to thermal expansion. The most tightly bonded hydroxyls escaped at \sim 600 °C and were completely depleted at 700 °C, again consistent with TGA-MS data (Chen et al. 2021). The long Fe-O bond length again decreased between 600 and 700 °C, whereas Fe-Fe distances hardly changed. The final decrease in the long Fe-O bond length (Fig. 10) may be related to the loss of magnetic coupling around the Néel temperature (T_N) at \sim 690 °C (Lu and Meng 2010).

The overall increase in Fe occupancies during the transformation from hydrohematite to stoichiometric hematite suggests that some hydrohematite steadily disintegrated and supplied the residual crystalline material with Fe. The breakdown of some hydrohematite into an amorphous phase was evidenced by a continual decrease in scale factor during the heating experiment (Fig. 10a). Moreover, we observed a slight increase in the background between 2θ of 8.3° and 13.8° (d-spacings of 5.7 to 3.4 Å) (Fig. 9).

DISCUSSION

Conditions for hydrohematite formation

Past researchers have reported hydrohematite as an unstable intermediate phase in the transformation of Fe-deficient to stoichiometric hematite (Wolska 1981; Wolska and Schwertmann 1989; Kustova et al. 1992; Gualtieri and Venturelli 1999; Liu et al. 2013; Peterson et al. 2015, 2016, 2018). It was not clear whether, under certain conditions, hydrohematite could be generated as a steady-state metastable product in preference to stoichiometric hematite. In the present work, we have successfully synthesized metastable hydrohematite from ferrihydrite at

pH 10 and 11 as an end-stage material. Peterson et al. (2018) also described an increase in refined Fe occupancies from 0.6 to 1.0 during the synthesis of hematite (Fig. 12). However, that study employed a different reactant (akageneite) at a very low starting pH (~1.0). We used fresh 2-line ferrihydrite as the starting material because ferrihydrite is the most common precursor to hematite and goethite in soils (Fischer and Schwertmann 1975; Schwertmann and Murad 1983; Paterson 1999; Waychunas et al. 2005; Colombo et al. 2014; Lagroix et al. 2016). We argue that high pH may be necessary to crystallize Fe-deficient hydrohematite as a steady-state product, at least when temperatures are above 25 °C. High OH⁻ concentrations in alkaline solutions may stabilize hydrous hydrohematite relative to anhydrous hematite. Thus, our results suggest hydrohematite preferentially precipitates in moderately alkaline, low-temperature fluids.

Structural mechanism of metastable hydrohematite crystallization

Classical crystal growth theories assume atom-by-atom or molecule-by-molecule attachment to the surface of a crystal growing in solution (Karthika et al. 2016). Schwertmann and Murad (1983) first proposed a departure from this simple mechanism by asserting that hematite forms through ferrihydrite aggregation and "internal structural re-arrangement." However, the nature of this structural change was not explained. We propose that the initially Fe-deficient structure of hydrohematite is inherited from precursor ferrihydrite through a rapid aggregation of ferrihydrite nanoparticles, consistent with the models of Soltis and Penn (2016) and Soltis et al. (2016). These authors report that trace amounts of defect-rich hematite nanoparticles were already detectable using low-temperature SQuID magnetometry in as-prepared 2-line ferrihydrite, even though hematite peaks were not visible by synchrotron XRD. Hematite growth occurred by "a particle-mediated growth mechanism," possibly involving

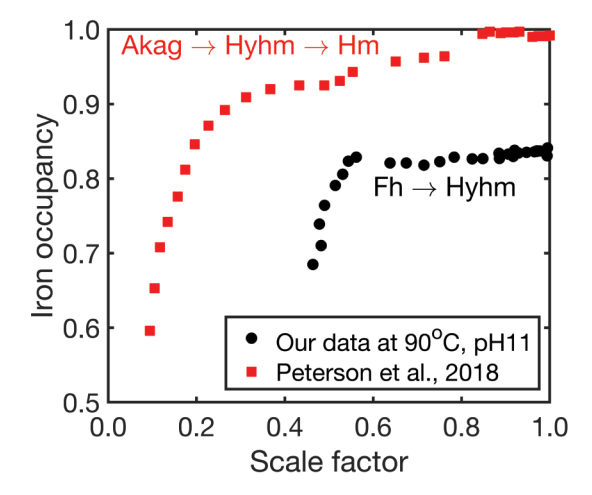


FIGURE 12. A comparison of the formation of hydrohematite from ferrihydrite in our study (Chen et al. 2021) and hematite formation from akageneite in Peterson et al. (2018). The variation in Fe occupancy in hematite is shown as a function of final phase abundance (as represented by final refined scale factors). Akageneite powders in solution were heated to 175 °C at pH 1.4 (red squares), whereas the ferrihydrite gels were heated in this study to 90 °C at pH 11. (Color online.)

oriented aggregation of hematite nanoparticles.

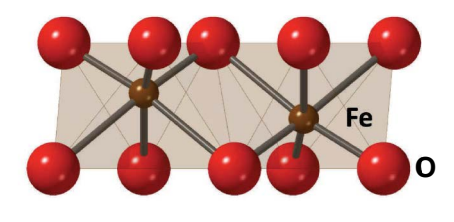
As these nanocrystals grow, we infer that Fe from dissolving or transforming 2-line ferrihydrite infills the defective hematite nanocrystals by vacancy diffusion, leading to an increase in Fe occupancy in the hematite. Since X-rays average over domains that are roughly 10 times the lattice repeat, it is useful to note that the low-Fe occupancies that we observed represent at least nanoscale-sized domains; aggregates of defect-free nanocrystals separated by Fe-deficient grain boundaries produced during oriented aggregation would not have yielded the XRD patterns that we observed. As more Fe infills the vacancies, stronger Fe-Fe repulsion leads to an increase in the Fe-Fe distances of face-sharing and edge-sharing octahedra and, therefore, an expansion in the lattice parameters. As the Fe occupancy reaches steady-state equilibrium (Fe_{occ} ~0.85), the Fe occupancy ceases to change, but the crystals can continue to grow. Thus, we suggest that hydrohematite forms through a non-classical process in which nanocrystal-mediated growth is accompanied by the infilling of vacancies with Fe.

Hydrogen positions

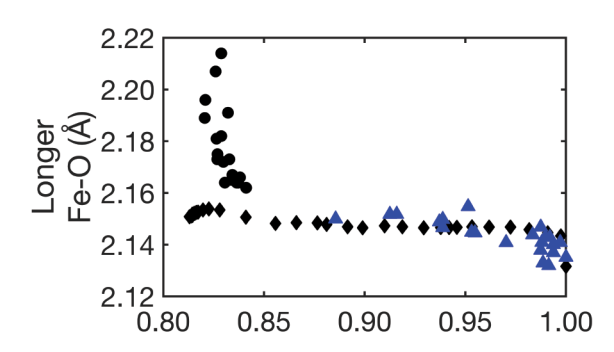
Due to the low-X-ray scattering factor for H⁺, the locations of the hydroxyl groups cannot be directly detected by XRD. However, our present study may offer some constraints with respect to the H positions in the hydrohematite structure: (1) the H atoms likely are bonded to the three longer Fe-O bonds; (2) the continuous loss of H on heating to 700 °C suggests that hydrohematite contains various hydroxyl bonding environments; and (3) high-activation energy is required to completely deprotonate the structure. Indeed, prior studies have reported that temperatures >1000 °C were required to remove all hydroxyls from synthetic hydrohematite (Wolska 1981; Wolska and Schwertmann 1989).

Figure 13 shows the relationship between Fe-O bond length and Fe occupancy when our hydrothermal and dry heating data sets are combined. Although mixing of these data sets does not account for the different thermal regimes of the wet and dry heating experiments, the results do suggest that decreasing Fe occupancies—and greater hydroxyl contents—lead to longer "long Fe-O bonds" and shorter "short Fe-O bonds" (Fig. 13). Thus, our heating data are consistent with trends described in Gualtieri and Venturelli (1999). As we ponder the peculiar metastability of hydrohematite when Fe_{occ} = 0.85, it is interesting to note the near constancy in the long Fe-O distance as Fe_{occ} increases from 0.85 to 1.00.

XRD patterns of the hydrohematite produced from ferrihydrite in this study did not exhibit extra reflections or split peaks. Indeed, despite the proposed existence of monoclinic "clinohematite" when akageneite transforms at low pH (Peterson et al. 2015), none of the synthetic hematite in the current study supported a departure from $R\overline{3}c$ symmetry. Thus, the incorporation of considerable concentrations of H in the hematite structure does not require a violation of the $R\overline{3}c$ symmetry. One may interpret the absence of superstructures as evidence that the vacancies, and also the H positions, lack long-range order. On the other hand, neutron scattering analyses do offer evidence for partial positional ordering of H, with approximately half of the H ordered and half disordered (Chen 2021). TGA-MS analyses of hydrohematite, as described in Chen et al. (2021), reveal a



- Fh to Hyhm
- Hyhm to HmGualtieri and Venturelli, 1999



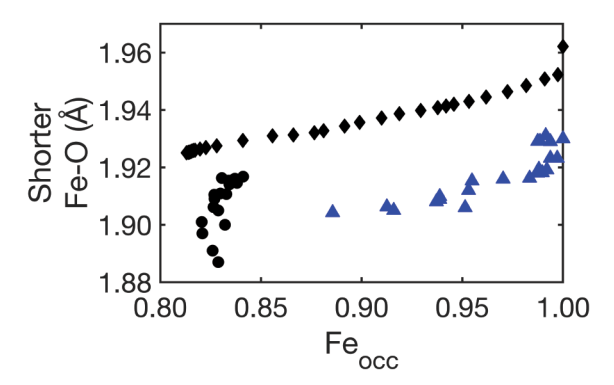


FIGURE 13. Fe-O bond length dependence on Fe occupancy, combining the data from the transformation of ferrihydrite (Fh) to hydrohematite (Hyhm) at 90 °C and pH 11, hydrohematite to hematite (Hm) from room temperature to 700 °C, and goethite to hematite from 200 to 800 °C (Gualtieri and Venturelli 1999). With an increased Fe occupancy, the three longer Fe-O bonds shorten, and the three shorter Fe-O bonds lengthen. (Color online.)

thermally continuous depletion of H as seen with TRXRD of heated samples and consistent with locally ordered OH groups with different bonding environments.

IMPLICATIONS

Our crystallographic analysis alters the conventional view of the crystallization mechanism for hematite and perhaps other metal hydroxides. Our XRD results reflect changes in the state of the bulk structure as hematite nanoparticles nucleated and grew. Importantly, the TRXRD data were insensitive to surface structures. Consequently, the observation of non-unitary occupancy factors for Fe reflects deficiencies within the inner volumes of

the nanoparticles. Thus, these experiments demonstrate that the hydrothermal transformation of ferrihydrite first generates hematite nanoparticles that are a crystallographic "Swiss cheese." The overall space group symmetry and atomic structure conform to those of hematite, but the vacancy concentrations of the first nanocrystals were so high that the compositions fell between Hm-Fe(OH) $_3$ and Hm-FeOOH (Fig. 1). The evolution of these highly Fe-deficient phases toward Fe $_2$ O $_3$ must involve rapid diffusion of Fe into interior sites. This study demonstrates the reach of in situ synchrotron X-ray diffraction coupled with Rietveld analysis to unravel the transformation mechanisms of minerals in hydrothermal systems.

Chen et al. (2021) report the widespread occurrence of natural hydrohematite with Fe occupancies near 0.85. Here, we provide a recipe to synthesize Fe-deficient hematite as a metastable product. Combining the natural discoveries of hydrohematite (Chen et al. 2021) and our laboratory synthesis of hydrohematite, we interpret our results to indicate that hydrohematite may form in alkaline and low-temperature solutions in sedimentary and hydrothermal deposits. Moreover, the Fe occupancy in hydrohematite and the hematite-to-goethite ratio are sensitive to pH and temperature, thus serving as a possible indicator of paleoclimatic conditions. Since the concentration of Fe vacancies in hematite can significantly modify its physical and chemical properties, such as color, magnetic properties, reactivity, and electrochemistry (Paterson 1999; Walter 2006; Lu et al. 2014; McBriarty et al. 2018; Guo et al. 2020), this study provides direction for the synthesis of hydrohematite with tailored characteristics. By extension, these results offer technological as well as natural implications, as they suggest that hydrohematite rather than hematite can form through watersaturated corrosion reactions at moderately alkaline pH, such as in the passivation layers on steel reinforcement in concrete (Leek 1991; Angst et al. 2017).

ACKNOWLEDGMENTS

We thank Nancy Lazarz at GSECARS BM-13 for her invaluable assistance in arranging for data collection at the beamline. We thank three anonymous reviewers and the associate editor who handled this paper for their helpful suggestions and comments.

FUNDING

Funding for this research was provided by National Science Foundation Grant EAR-1552211 and EAR-1925903, the Pennsylvania State University Biogeochemistry dual-title Ph.D. program, and the Hiroshi and Koya Ohmoto Graduate Fellowship of Pennsylvania State University Geosciences Department. Synchrotron XRD was performed at GSECARS (University of Chicago) Beamline 13-BM-C at the APS. GSECARS is supported by NSF EAR-1634415 and DOE GeoSciences DE-FG02-94ER14466. A.P.S. is operated under DOE Contract No. DE-AC02-06CH11357.

REFERENCES CITED

Angst, U.M., Geiker, M.R., Michel, A., Gehlen, C., Wong, H., Isgor, O.B., Elsener, B., Hansson, C.M., François, R., Hornbostel, K., and others. (2017) The steel-concrete interface. Materials and Structures, 50, 143, https://doi.org/10.1617/s11527-017-1010-1.

Bagheri, S., Chandrappa, K.G., and Hamid, S.B.A. (2013) Generation of Hematite Nanoparticles via Sol-Gel Method. Research Journal of Chemical Sciences, 3, 62–68.

Barrón, V. and Torrent, J. (2013) Iron, manganese and aluminium oxides and oxyhydroxides. In F. Nieto, K.J.T. Livi, and R. Oberti, Eds., Minerals at the Nanoscale, p. 297–336. Mineralogical Society of Great Britain and Ireland.

Barrón, V., Torrent, J., and de Grave, E. (2003) Hydromaghemite, an intermediate in the hydrothermal transformation of 2-line ferrihydrite into hematite. American Mineralogist, 88, 1679–1688, https://doi.org/10.2138/am-2003-11-1207.

Blake, R.L., Hessevic, K.R.E., Zoltai, T., and Finger, L.W. (1966) Refinement of

- the hematite structure. American Mineralogist, 51, 123-129.
- Breithaupt, J.F.A. (1847) Vollständiges handbuch der mineralogie, vol. 3, Arnoldische Buchhandlung, Arnoldische Buchhandlung.
- Burgina, E.B., Kustova, G.N., Tsybulya, S.V., Kryukova, G.N., Litvak, G.S., Isupova, L.A., and Sadykov, V.A. (2000) Structure of the metastable modification of iron(III) oxide. Journal of Structural Chemistry, 41, 396–402, https://doi.org/10.1007/BF02741997.
- Cao, L., Jiang, Z.-X., Du, Y.-H., Yin, X.-M., Xi, S.-B., Wen, W., Roberts, A.P., Wee, A.T.S., Xiong, Y.-M., Liu, Q.-S., and others. (2017) Origin of magnetism in hydrothermally aged 2-line ferrihydrite suspensions. Environmental Science & Technology, 51, 2643–2651, https://doi.org/10.1021/acs.est.6b04716.
- Chen, S.A. (2021) The formation of iron (hydr)oxides in surface environments: A crystallographic and kinetic study. Ph.D. thesis, Pennsylvania State University, University Park.
- Chen, S.A., Heaney, P.J., Post, J.E., Fischer, T.B., Eng, P.J., and Stubbs, J.E. (2021) Superhydrous hematite and goethite: A potential water reservoir in the red dust of Mars? Geology, 49, 1343–1347, https://doi.org/10.1130/G48929.1.
- Chen, S.A., Heaney, P.J., Post, J.E., Eng, P.J., and Stubbs, J.E. (2022) Hematite-goethite ratios at pH 2–13 and 70–170 °C: A time-resolved synchrotron X-ray diffraction study. Chemical Geology, 606, 120995, https://doi.org/10.1016/j.chemgeo.2022.120995.
- Claudio, C., Iorio, E.D., Liu, Q., Jiang, Z., and Barrón, V. (2017) Iron oxide nanoparticles in soils: Environmental and agronomic importance. Journal of Nanoscience and Nanotechnology, 17, 4449–4460, https://doi.org/10.1166/ jnn.2017.14197.
- Colombo, C., Palumbo, G., He, J.Z., Pinton, R., and Cesco, S. (2014) Review on iron availability in soil: Interaction of Fe minerals, plants, and microbes. Journal of Soils and Sediments, 14, 538–548, https://doi.org/10.1007/s11368-013-0814-z.
- Cornell, R.M. and Schwertmann, U. (2003) The Iron Oxides: structure, properties, reactions, occurrences, and uses (Vol. 664). Wiley.
- Das, S., Hendry, M.J., and Essilfie-Dughan, J. (2011) Transformation of two-line ferrihydrite to goethite and hematite as a function of pH and temperature. Environmental Science & Technology, 45(1), 268–275.
- Diehm, P.M., Ágoston, P., and Albe, K. (2012) Size-dependent lattice expansion in nanoparticles: reality or anomaly? ChemPhysChem, 13(10), 2443–2454.
- Fischer, W.R. and Schwertmann, U. (1975) The formation of hematite from amorphous iron(III)hydroxide. Clays and Clay Minerals, 23, 33–37, https:// doi.org/10.1346/CCMN.1975.0230105.
- Fischer, T.B., Heaney, P.J., and Post, J.E. (2018) Changes in the structure of birnessite during siderophore-promoted dissolution: A time-resolved synchrotron X-ray diffraction study. Chemical Geology, 476, 46–58, https://doi.org/10.1016/j.chemgeo.2017.11.003.
- Gates-Rector, S. and Blanton, T. (2019) The Powder Diffraction File: A quality materials characterization database. Powder Diffraction, 34, 352–360, https:// doi.org/10.1017/S0885715619000812.
- Gualtieri, A.F. and Venturelli, P. (1999) In situ study of the goethite-hematite phase transformation by real time synchrotron powder diffraction. American Mineralogist, 84, 895–904, https://doi.org/10.2138/am-1999-5-624.
- Guo, S.Q., Hu, Z.Z., Zhen, M.M., Gu, B.C., Shen, B.X., and Dong, F. (2020) Insights for optimum cation defects in photocatalysis: A case study of hematite nanostructures. Applied Catalysis B: Environmental, 264, 118506, https://doi.org/ 10.1016/j.apcatb.2019.118506.
- Haavik, C., Stølen, S., Fjellvåg, H., Hanfland, M., and Häusermann, D. (2000) Equation of state of magnetite and its high-pressure modification: Thermodynamics of the Fe-O system at high pressure. American Mineralogist, 85, 514–523, https://doi.org/10.2138/am-2000-0413.
- Hahn, B.P., Long, J.W., Mansour, A.N., Pettigrew, K.A., Osofsky, M.S., and Rolison, D.R. (2011) Electrochemical Li-ion storage in defect spinel iron oxides: The critical role of cation vacancies. Energy & Environmental Science, 4, 1495–1502, https://doi.org/10.1039/c0ee00819b.
- Heaney, P.J., Oxman, M.J., and Chen, S.A. (2020) A structural study of size-dependent lattice variation: In situ X-ray diffraction of the growth of goethite nanoparticles from 2-line ferrihydrite. American Mineralogist, 105, 652–663, https://doi.org/10.2138/am-2020-7217.
- Hermann R. (1844) Untersuchungen russischer Mineralien. Journal f
 ür Praktische Chemie, 33, 87–98.
- Hill, A.H., Jiao, F., Bruce, P.G., Harrison, A., Kockelmann, W., and Ritter, C. (2008) Neutron diffraction study of mesoporous and bulk hematite, α-Fe₂O₃. Chemistry of Materials, 20, 4891–4899, https://doi.org/10.1021/cm800009s.
- Hu, Z., Shen, Z., and Yu, J.C. (2016) Covalent fixation of surface oxygen atoms on hematite photoanode for enhanced water oxidation. Chemistry of Materials, 28, 564–572, https://doi.org/10.1021/acs.chemmater.5b04058.
- Hyland, E.G., Sheldon, N.D., Van der Voo, R., Badgley, C., and Abrajevitch, A. (2015) A new paleoprecipitation proxy based on soil magnetic properties: Implications for expanding paleoclimate reconstructions. Geological Society of America Bulletin, 127, 975–981, https://doi.org/10.1130/B31207.1.
- Ji, J., Chen, J., Balsam, W., Lu, H., Sun, Y., and Xu, H. (2004) High resolution hematite/goethite records from Chinese loess sequences for the last glacialinterglacial cycle: Rapid climatic response of the East Asian Monsoon to the

- tropical Pacific. Geophysical Research Letters, 31, L03207, https://doi.org/10.1029/2003GL018975.
- Jiang, Z., Liu, Q., Roberts, A.P., Dekkers, M.J., Barrón, V., Torrent, J., and Li, S. (2022) The magnetic and color reflectance properties of hematite: From Earth to Mars. Reviews of Geophysics, 60, e2020RG000698.
- Karthika, S., Radhakrishnan, T.K., and Kalaichelvi, P. (2016) A review of classical and non-classical nucleation theories. Crystal Growth & Design, 16, 6663–6681, https://doi.org/10.1021/acs.cgd.6b00794.
- Kim, C.Y. (2020) Atomic structure of hematite (α-Fe₂O₃) nanocube surface; synchrotron X-ray diffraction study. Nano-Structures and Nano-Objects, 23, 100497, https://doi.org/10.1016/j.nanoso.2020.100497.
- Kustova, G.N., Burgina, E.B., Sadykov, V.A., and Poryvaev, S.G. (1992) Vibrational spectroscopic investigation of the goethite thermal decomposition products. Physics and Chemistry of Minerals, 18, 379–382, https://doi.org/10.1007/ BF00199419.
- Lagroix, F., Banerjee, S.K., and Jackson, M.J. (2016) Geological occurrences and relevance of iron oxides. In D. Faivre, Ed., Iron Oxides: From Nature to Applications, 7–29. Wiley-VCH.
- Larson, A.C. and Von Dreele, R.B. (2000) General Structure Analysis System, LAUR 86-748 p. Los Alamos National Laboratory.
- Leek, D.S. (1991) The passivity of steel in concrete. Quarterly Journal of Engineering Geology, 24, 55–66, https://doi.org/10.1144/GSL.QJEG.1991.024.01.05.
- Liu, H., Chen, T., Zou, X., Qing, C., and Frost, R.L. (2013) Thermal treatment of natural goethite: Thermal transformation and physical properties. Thermochimica Acta, 568, 115–121, https://doi.org/10.1016/j.tca.2013.06.027.
- Løvlie, R., Torsvik, T., Jelenska, M., and Levandowski, M. (1984) Evidence for detrital remanent magnetization carried by hematite in Devonian red beds from Spitsbergen: Palaeomagnetic implications. Geophysical Journal International, 79, 573–588, https://doi.org/10.1111/j.1365-246X.1984.tb02242.x.
- Lu, H.M. and Meng, X.K. (2010) Neel temperature of hematite nanocrystals. The Journal of Physical Chemistry C, 114, 21291–21295, https://doi.org/10.1021/ jp108703b.
- Lu, X., Zeng, Y., Yu, M., Zhai, T., Liang, C., Xie, S., Balogun, M.S., and Tong, Y. (2014) Oxygen-deficient hematite nanorods as high-performance and novel negative electrodes for flexible asymmetric supercapacitors. Advanced Materials, 26, 3148–3155, https://doi.org/10.1002/adma.201305851.
- McBriarty, M.E., Kerisit, S., Bylaska, E.J., Shaw, S., Morris, K., and Ilton, E.S. (2018) Iron vacancies accommodate uranyl incorporation into hematite. Environmental Science & Technology, 52, 6282–6290, https://doi.org/10.1021/ acs.est.8b00297.
- Paterson, E. (1999) The iron oxides. Structure, properties, reactions, occurrences and uses. Clay Minerals, 34, 209–210.
- Perebeinos, V., Chan, S.W., and Zhang, F. (2002) 'Madelung model' prediction for dependence of lattice parameter on nanocrystal size. Solid State Communications, 123(6-7), 295–297.
- Peterson, K.M., Heaney, P.J., Post, J.E., and Eng, P.J. (2015) A refined monoclinic structure for a variety of "hydrohematite". American Mineralogist, 100, 570–579, https://doi.org/10.2138/am-2015-4807.
- Peterson, K.M., Heaney, P.J., and Post, J.E. (2016) A kinetic analysis of the transformation from akaganeite to hematite: An in situ time-resolved X-ray diffraction study. Chemical Geology, 444, 27–36, https://doi.org/10.1016/j. chemgeo.2016.09.017.
- Peterson, K.M., Heaney, P.J., and Post, J.E. (2018) Evolution in the structure of akaganeite and hematite during hydrothermal growth: An in situ synchrotron X-ray diffraction analysis. Powder Diffraction, 33, 287–297, https://doi.org/10.1017/S0885715618000623.
- Post, J.E. and Bish, D.L. (1989) Rietveld refinement of crystal structures using powder X-ray diffraction data. Reviews in Mineralogy and Geochemistry, 20, 277–308.
- Prescher, C. and Prakapenka, V.B. (2015) DIOPTAS: A program for reduction of two-dimensional X-ray diffraction data and data exploration. High Pressure Research, 35, 223–230, https://doi.org/10.1080/08957959.2015.1059835.
- Scherrer, P. (1918) Bestimmung der Grosse und inneren Struktur von Kolloidteilchen mittels Rontgenstrahlen. Nach Ges Wiss Gottingen, 2, 8–100.
- Schwertmann, U. and Murad, E. (1983) Effect of pH on the formation of goethite and hematite from ferrihydrite. Clays and Clay Minerals, 31, 277–284, https:// doi.org/10.1346/CCMN.1983.0310405.
- Soltis, J.A. and Penn, R.L. (2016) Oriented attachment and non-classical formation in iron oxides. In D. Faivre, Ed., Iron Oxides: From Nature to Applications, 243–268. Wiley-VCH.
- Soltis, J.A., Feinberg, J.M., Gilbert, B., and Penn, R.L. (2016) Phase transformation and particle-mediated growth in the formation of hematite from 2-line ferrihydrite. Crystal Growth & Design, 16, 922–932, https://doi.org/10.1021/ acs.cgd.5b01471.
- Szaniawski, R., Ludwiniak, M., and Rubinkiewicz, J. (2012) Minor counterclock-wise rotation of the Tatra Mountains (Central Western Carpathians) as derived from paleomagnetic results achieved in hematite-bearing Lower Triassic sandstones. Tectonophysics, 560–561, 51–61, https://doi.org/10.1016/j.tecto.2012.06.027.

- Thompson, P., Cox, D.E., and Hastings, J.B. (1987) Rietveld refinement of Debye–Scherrer synchrotron X-ray data from Al₂O₃. Journal of Applied Crystallography, 20, 79–83, https://doi.org/10.1107/S0021889887087090.
- Toby, B.H. and Von Dreele, R.B. (2013) GSAS-II: The genesis of a modern open-source all purpose crystallography software package. Journal of Applied Crystallography, 46, 544–549, https://doi.org/10.1107/S0021889813003531.
- Walker, T.R., Larson, E.E., and Hoblitt, R.P. (1981) Nature and origin of hematite in the Moenkopi Formation (Triassic), Colorado Plateau: A contribution to the origin of magnetism in red beds. Journal of Geophysical Research, 86 (B1), 317–333, https://doi.org/10.1029/JB086iB01p00317.
- Walter, D. (2006) Characterization of synthetic hydrous hematite pigments. Thermochimica Acta, 445, 195–199, https://doi.org/10.1016/j.tca.2005.08.011.
- Wang, S., Gao, B., Zimmerman, A.R., Li, Y., Ma, L., Harris, W.G., and Migliaccio, K.W. (2015) Removal of arsenic by magnetic biochar prepared from pinewood and natural hematite. Bioresource Technology, 175, 391–395, https://doi.org/ 10.1016/j.biortech.2014.10.104.
- Waychunas, G.A., Kim, C.S., and Banfield, J.F. (2005) Nanoparticulate iron oxide minerals in soils and sediments: Unique properties and contaminant scavenging mechanisms. Journal of Nanoparticle Research, 7, 409–433, https://doi.org/ 10.1007/s11051-005-6931-x.
- Wolska, E. (1981) The structure of hydrohematite. Zeitschrift für Kristallographie, 154, 69–76, https://doi.org/10.1524/zkri.1981.154.14.69.
- —— (1988) Relations between the existence of hydroxyl ions in the anionic sublattice of hematite and its infrared and X-ray characteristics. Solid State

- Ionics, 28–30, 1349–1351, https://doi.org/10.1016/0167-2738(88)90385-2.
 Wolska, E. and Schwertmann, U. (1989) Nonstoichiometric structures during dehydroxylation of goethite. Zeitschrift für Kristallographie, 189, 223–237, https://doi.org/10.1524/zkri.1989.189.3-4.223.
- Yang, T.Y., Kang, H.Y., Sim, U., Lee, Y.J., Lee, J.H., Koo, B., Nam, K.T., and Joo, Y.C. (2013) A new hematite photoanode doping strategy for solar water splitting: Oxygen vacancy generation. Physical Chemistry Chemical Physics, 15, 2117–2124, https://doi.org/10.1039/c2cp44352j.

Manuscript received November 5, 2021 Manuscript accepted October 18, 2022 Accepted Manuscript online October 27, 2022 Manuscript Handled by Maarten A.T.M. Broekmans

Endnote:

Deposit item AM-23-98379. Online Materials are free to all readers. Go online, via the table of contents or article view, and find the tab or link for supplemental materials. The CIF has been peer-reviewed by our Technical Editors.